



INSTITUT DE FRANCE
Académie des sciences

Comptes Rendus

Géoscience

Sciences de la Planète

Laurent Cormier, Louis Hennet, Gerald Lelong, Gabriel J. Cuello
and Alexei Bytchkov

Structure from glass to melt: a case study along the MgSiO_3 – CaSiO_3 join using neutron and X-ray diffraction

Volume 354, Special Issue S1 (2022), p. 15-34


Published online: 16 March 2022

Issue date: 29 May 2023

<https://doi.org/10.5802/crgeos.112>

Part of Special Issue: Glass, an ubiquitous material

Guest editor: Daniel Neuville (Université de Paris, Institut de physique du globe de Paris, CNRS)

 This article is licensed under the
CREATIVE COMMONS ATTRIBUTION 4.0 INTERNATIONAL LICENSE.
<http://creativecommons.org/licenses/by/4.0/>



*Les Comptes Rendus. Géoscience — Sciences de la Planète sont membres du
Centre Mersenne pour l'édition scientifique ouverte*

www.centre-mersenne.org

e-ISSN : 1778-7025



Glass, an ubiquitous material / *Le verre, un matériau omniprésent*

Structure from glass to melt: a case study along the MgSiO₃–CaSiO₃ join using neutron and X-ray diffraction

Laurent Cormier^{®*, a}, Louis Hennet^{® b}, Gerald Lelong^{® a}, Gabriel J. Cuello^{® c}
and Alexei Bytchkov^{® d}

^a Sorbonne Université, Muséum National d'Histoire Naturelle, UMR CNRS 7590, IRD, Institut de Minéralogie, de Physique des Matériaux et de Cosmochimie, IMPMC, 75005 Paris, France

^b ICMN, CNRS, University of Orleans, 45071 Orléans, France

^c Institut Laue-Langevin, 38042 Grenoble, France

^d European Synchrotron Radiation Facility (ESRF), 38043 Grenoble, France

E-mails: laurent.cormier@sorbonne-universite.fr (L. Cormier), louis.hennet@cns-orleans.fr (L. Hennet), gerald.lelong@sorbonne-universite.fr (G. Lelong), cuello@ill.fr (G. Cuello), aleksei.bychkov@gmail.com (A. Bytchkov)

Abstract. Glass and melt structures are inherently complex and disordered with significant changes expected to occur with temperature. In the present paper, a comparison of the structure of glasses and liquids along the MgSiO₃–CaSiO₃ join is carried out using neutron and X-ray diffraction (XRD). Empirical Potential Structure Refinement (EPSR) simulations were used to fit the experimental data. The average coordination number (CN) and site distribution is obtained for Mg and Ca showing distinct sites between the two cations and higher coordinated sites in the liquids. The major glass to melt modifications is observed at the scale of intermediate range order (IRO) by rearrangement of the (Ca,Mg)–Si and (Ca,Mg)–(Ca,Mg) connections. The structural evolution with temperature, especially concerning the cationic environments, illustrates the differences between glass and melt organization. These changes highlight the important contribution of cations to thermodynamical properties, diffusion and glass forming ability.

Keywords. Glass, Structure, Diffraction, Modelling, Coordination, Topology.

Published online: 16 March 2022, *Issue date:* 29 May 2023

1. Introduction

The structure of silicate melts is of considerable importance in igneous processes and in industrial applications (furnace conditions) as the atomic-scale

organization strongly affects their dynamical and physico-chemical properties (for instance, density, entropy, crystal-melt element partitioning and transport properties including viscosity and diffusivity). Glasses have long been acknowledged as good analogues of liquids with a structure that can be easily revealed experimentally. On the contrary, measure-

* Corresponding author.

ments at elevated temperatures can be challenging and can give less detailed structural information. However, important changes in properties occur above the glass transition temperature, T_g , such as an increase in heat capacity and thermal expansivity, a decrease in viscosity, etc. These observations imply that the glass structure reflects only the supercooled liquid structure frozen in at T_g with, additionally, a strong dependence due to the thermal history, i.e. typically the quenching rate [Allwardt and Stebbins, 2004, Henderson et al., 2006]. Therefore, glasses may show significant structural differences compared to high-temperature liquids. To understand how data obtained on glasses can be extrapolated to melts, it is pertinent to track how the structure evolves with temperature, how fast the structural changes happen and how they can affect bulk properties [Stebbins, 2008].

Liquids and glasses are both characterized by a lack of long range order. Unlike crystals for which a unique, accurate structural model can be established, the glass/melt structure is described statistically, by considering average information on the structure extending over short and intermediate range scale, referred to as SRO (short range order) and IRO. Among the many experimental tools allowing the elucidation of the complexity of silicate glasses/melts, X-ray and neutron diffraction offer the possibility to probe both SRO and IRO [Cormier, 2019, Cormier et al., 2001, Wilding and Benmore, 2006] and benefits from the availability of high-temperature devices [Cuello et al., 2014, Skinner et al., 2012]. Diffraction gives access to a pair distribution function (PDF) in real space that is the probability of finding an atom at a distance r from an atom taken at the origin. In addition to experimental data, a structural description provided by modelling approaches is usually required to reveal many structural aspects. This can be readily obtained from diffraction data using methods such as reverse Monte Carlo (RMC) or Empirical Potential Structure Refinement (EPSR) [Majerus et al., 2004, Nienhuis et al., 2021]. Comparatively to glasses, structural data for liquids are lacking, which preclude an evaluation of the glass/melt comparison and do not offer experimental validation for developing new, more accurate potentials in molecular dynamics (MD) simulations [Shih et al., 2021].

The $\text{MgSiO}_3\text{-CaSiO}_3$ (CMS) join is a simple sys-

tem with two non-network forming cations (Mg, Ca), and having a complete glass formation region between the two end members, MgSiO_3 and CaSiO_3 . It contains three minerals of interest to the geochemistry of upper mantle, enstatite (MgSiO_3), diopside ($\text{CaMgSi}_2\text{O}_6$) and wollastonite (CaSiO_3). Enstatite and diopside are pyroxene minerals [Thompson and Downs, 2004, 2003]. Their structure consists of single-chains of corner-sharing SiO_4 tetrahedra. These chains are connected by their apices to regular octahedral M1 sites that form a chain of edge-shared octahedra. Parallel to the M1 chains, there is a second octahedral chain with M2 sites that are larger and more distorted than M1 sites enabling the introduction of large cations. In diopside, Ca atoms fill the large M2 sites while Mg atoms fill the regular M1 sites. Due to its size, Ca atoms cannot be accommodated in M1 sites so that CaSiO_3 has a slightly different structure and is referred as a pyroxenoid. In wollastonite [Hesse, 1984, Trojer, 1968], the tetrahedral chain periodicity is modified (3 repeat SiO_4 rather than 2 repeat SiO_4 for pyroxenes) to allow Ca entering M1-type sites. This results in a lower crystal symmetry.

The Ca-Mg mixing in glasses/melts adds complexity to the structure with possible evolution with temperature. As the cations have the same nominal electric charge but different cationic size ($r_{\text{Mg}^{2+}} = 0.71 \text{ \AA}$, $r_{\text{Ca}^{2+}} = 1.14 \text{ \AA}$ [Shannon, 1976]), distinct site preferences are expected and local coordination change or local site distortion could arise with temperature. Ca-Mg mixing along the $\text{MgSiO}_3\text{-CaSiO}_3$ join yields a non-linear variation of the viscosity, with a lower viscosity (at a given temperature) for the diopside composition compared to either end members and a minima that is enhanced near T_g [Neuville and Richet, 1991]. The authors have shown that this behavior can be interpreted by an excess in configurational entropy for the liquids implying ideal cation mixing behavior. Much of the excess entropy is retained in intermediate compositions at T_g . Structural analysis of CMS glasses support random cation mixing as these compounds are described with a disordered distribution of Ca and Mg cations [Allwardt and Stebbins, 2004, Cormier et al., 2010]. Though glasses in this system have been widely investigated [Cormier and Cuello, 2012, 2011, De Sousa Meneses et al., 2006, Gaskell et al., 1991, Kalampounias et al., 2009, Kohara et al., 2011, Kroeker and Stebbins, 2000,

Table 1. Composition (in mol%, ± 0.05) and density, d (in $\text{g}\cdot\text{cm}^{-3}$, ± 0.002) for the $\text{CaO}_x \cdot \text{MgO}_{1-x} \cdot 2\text{SiO}_2$ glasses

Name	Nominal composition	SiO ₂	CaO	MgO	NBO/Q*	d_{glass} ($\text{g}\cdot\text{cm}^{-3}$)	d_{liquid} ($\text{g}\cdot\text{cm}^{-3}$)	T_{neutron} (K)	$T_{\text{X-ray}}$ (K)
CMS00.50 (enstatite composition)	MgO–SiO ₂	50.38	—	49.62	1.97	2.693	2.502 (1923 K)	1873	1973
CMS12.38	0.5CaO– 1.5MgO–2SiO ₂	49.60	14.08	36.32	2.03	2.789	2.547 (1773 K)		1773
CMS25.25 (diopside composition)	CaO–MgO– 2SiO ₂	50.24	25.33	25.32	2.02	2.805	2.563 (1873 K)	1673	1973
CMS38.12	1.5CaO– 0.5MgO–2SiO ₂	48.6	36.98	14.42	2.11	2.871	2.612 (1773)		1773
CMS50.00 (wollastonite composition)	CaO–SiO ₂	50.42	49.58	—	1.97	2.891	2.615 (1923 K)	1873	1973

*Number of non-bridging oxygen (NBO) per SiO₄ tetrahedra (Q), calculated with the formula $NBO/Q = (20 - 4Q)/Q$.

Schneider *et al.*, 2003, Shimoda *et al.*, 2008, 2007, Taniguchi *et al.*, 1997, 1995, Wilding *et al.*, 2004, Yin *et al.*, 1983, Zhang *et al.*, 1997], experimental studies in the liquid state are limited to MgSiO₃ [Wilding *et al.*, 2010, 2008] and CaSiO₃ [Benmore *et al.*, 2020, 2010, Skinner *et al.*, 2012]. It would thus be valuable to have further investigation of the molten structure of intermediate compositions, including the important diopside composition, for which entropic and structural effects are maximized.

In this paper, we aim to explore the structural evolution along the MgSiO₃–CaSiO₃ join using neutron diffraction (ND) and X-ray diffraction (XRD) at high temperature. The experimental data have been fitted using the EPSR approach to reveal structural differences between glasses and melts.

2. Experimental

2.1. Sample preparation

Glasses along the Ca–Mg pyroxene join ($\text{Ca}_x\text{Mg}_{1-x}\text{Si}_2\text{O}_6$, where $x = 0, 0.25, 0.5, 0.75$, and 1) were prepared from powders of SiO₂, CaCO₃ and MgO in high purity commercial forms. The decomposition of the carbonates was obtained by heating at 800 °C overnight. The mixtures were subsequently melted, at 100 °C above their respective melting temperatures, during 1 h in a Pt-10%Rh crucible. The glasses were obtained by quenching the

melts, dipping the bottom of the crucibles in water. The samples were crushed in an agate mortar and remelted two times to improve the glass chemical homogeneity. Glasses are labeled CMS $x.y$ where $x = \text{mol\% CaO}$, $y = \text{mol\% MgO}$ and $(100 - x - y) = \text{mol\% SiO}_2$.

Pieces of each glass were embedded in epoxy resin, polished, carbon-coated and chemically analyzed using an electron probe micro-analyzer (CAMECA SX50) at the Camparis Centre (Sorbonne Université, France), as reported previously [Cormier and Cuello, 2012]. The chemical compositions (Table 1) are obtained by averaging ten different points. Glass densities were measured at room temperature by the Archimedes method with toluene as immersion liquid. Melt densities were obtained or extrapolated from experimental data [Courtial and Dingwell, 1999, 1995]. Table 1 gives the densities and the experimental temperatures used in diffraction measurements.

2.2. X-ray diffraction

High energy XRD measurements were carried out at the beamline ID11 at the European Synchrotron Radiation Facility (ESRF) using an aerodynamic levitation and laser heating device [Drewitt *et al.*, 2011, Hennet *et al.*, 2011]. The synchrotron X-ray beam, $100 \times 100 \mu\text{m}^2$ in cross-sectional area and 100.456 keV in energy, was incident on the spherical

liquid droplets that are levitating above the nozzle of the levitator using an argon gas flow through an aluminum conical nozzle. Two 125 W CO₂ laser beams were used for heating, with temperatures measured at 1773 K (CMS00.50, CMS38.12, CMS50.00) or 1773 K (CMS12.38, CMS25.25). Two-dimensional diffraction patterns were recorded with ESRF-designed FReLoN CCD camera [Labiche *et al.*, 2007]. The scattered beam was positioned at the corner of the detector which allows a wide total scattering momentum (Q) range extending to $Q_{\max} = 23.6 \text{ \AA}^{-1}$. The sample-to-detector distances, beam center and detector tilt were determined by comparison between the known d -spacings of a Si calibrant. The diffraction data were flat-fielded and corrected for dark current noise, geometrical effects and incident beam polarization and reduced to one-dimensional patterns using FIT2D software. The measured diffracted intensities were scaled to fit the sum of the Compton and self-scattering, which was then subtracted to obtain the total structure factor $F^X(Q)$, using standard procedure [Drewitt *et al.*, 2013, 2011].

2.3. Neutron diffraction

The ND measurements were carried out on the D4C diffractometer at the Institut Laue-Langevin, using an aerodynamic levitation and laser heating device [Hennet *et al.*, 2006]. Acquisitions at high temperature were obtained on the liquid samples and the empty levitation device inside the diffraction chamber. A vanadium standard was also measured at room temperature for absolute normalization of the scattering intensity. The neutron wavelength was 0.4979 \AA^{-1} , giving a useable Q -range up to $Q_{\max} = 23.6 \text{ \AA}^{-1}$. The program CORRECT was used to process the data corrections for attenuation, background, multiple scattering and inelasticity effects [Howe *et al.*, 1996], giving the neutron total structure factor, $F^N(Q)$. The ambient ND data are those previously published, also acquired on the D4C diffractometer [Cormier *et al.*, 2010], except the CMS25.25 glass that has been measured during this experiment.

3. Empirical potential structure refinement

Structural models for the glasses and the liquids were derived from the diffraction data using EPSR [Soper, 2005]. This method refines atomic positions within

Table 2. Parameters for the reference potentials in EPSR simulations

Element	Electric charge	ϵ (kJ·mol ⁻¹)	σ (Å)
Si	+2	0.175	1.06
O	-1	0.1625	3.6
Mg	+1	0.2	1.8
Ca	+1	0.2	2.4

a box model and interatomic potentials between atomic pairs to progressively get an agreement between the simulated and measured diffraction data. The fitting procedure was performed simultaneously on the neutron and X-ray data for all glasses, while for the liquids only X-ray data were available for CMS12.38 and CMS38.12. The potential parameters used for EPSR modelling were determined as previously reported [Weigel *et al.*, 2008] and are given in Table 2. The atomic cubic box specifications are listed in Table 3. Initial random configurations of 5000 atoms were generated and equilibrated at room temperature (glass) or at high temperature (liquid) close to the experimental one, using the reference potential. Then, the empirical potentials were refined by variation of the requested energy amplitude (*ereq* values) between 0–50 kJ·mol⁻¹ in order to reproduce the experimental datasets. Once a good fit is obtained, with an equilibrated internal energy, statistical structural data were collected by averaging over ensembles of >1500 configurations.

4. Results

4.1. Structure factors

The experimental X-ray/neutron structure factors for the samples in the glass and liquid states are shown in Figure 1. As MgO is replaced by CaO in glasses, the position of the first peak, Q_p , in $F^N(Q)$ functions is shifted from $1.92 \pm 0.01 \text{ \AA}^{-1}$ for CMS00.50 to $2.05 \pm 0.01 \text{ \AA}^{-1}$ for CMS50.00, and the Q_p peak intensity slightly decreases. These positions are related to density fluctuations separated by a distance $d = 2\pi/Q_p$, giving values between $3.29 \pm 0.02 \text{ \AA}$ for CMS00.50 to $3.06 \pm 0.02 \text{ \AA}$ for CMS50.00. On melting, the Q_p peak is clearly shifted to lower Q -values, at

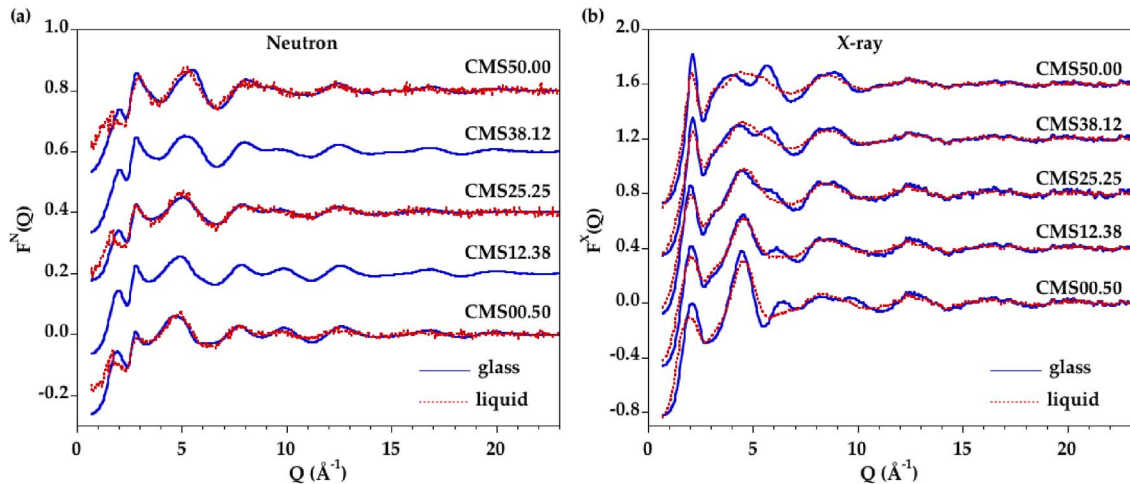


Figure 1. Comparison of the measured structure factors for the glasses and melts for (a) neutron and (b) X-ray diffraction. The blue solid curve is the glass and the dashed red curve is the liquid.

Table 3. Box lengths and densities of the EPSR models

Glass	Box length (Å)	Atomic number, ρ (atoms Å ⁻³)	$R_{\chi(\text{neutron})}$	$R_{\chi(\text{X-ray})}$	Temperature (K)
CMS00.50-glass	39.56	0.08076	0.222	0.431	300
CMS00.50-liquid	40.51	0.07503	0.339	0.265	1923
CMS12.38-glass	39.61	0.08048	0.124	0.339	300
CMS12.38-liquid	40.82	0.07349	—	0.132	1773
CMS25.25-glass	40.05	0.07781	0.212	0.603	300
CMS25.25-liquid	41.24	0.07126	0.369	0.549	1723
CMS38.12-glass	40.19	0.07702	—	0.359	300
CMS38.12-liquid	41.48	0.07008	0.088	0.210	1773
CMS50.00-glass	40.56	0.07493	0.050	0.272	300
CMS50.00-liquid	41.94	0.06777	0.247	0.286	1923

R_{χ} are reliability factors calculated in the real space over the range $1 \leq r \leq 8$ Å [Wright, 1993]. Temperatures used during simulations.

~ 1.67 Å⁻¹, but the low statistics does not allow to distinguish any compositional variations. This displacement implies higher correlation distances in the liquids compared to the glasses. This can be attributed either to a density effect (lower densities in the liquid state) or to structural changes. A similar peak is observed in $F^X(Q)$ functions for glasses and liquids and, in this case, a strong chemical dependence is observed: the intensity increases as more CaO is substituted to MgO. Additionally, the peak position shifts from 2.04 ± 0.02 Å⁻¹ to 2.12 ± 0.01 Å⁻¹ in glasses with increasing CaO content and from 1.98 ± 0.02 Å⁻¹ to 2.15 ± 0.02 Å⁻¹ in liquids with increasing CaO content.

This peak is thus particularly sensitive to cation organization.

For both neutron and X-ray datasets, the presence of isobestic points (common points in the diffraction patterns) is observed for the glass and the melt series (Supplementary Figure S1). These points indicate that $F^N(Q)$ or $F^X(Q)$ functions for intermediate compositions can be obtained using a linear combination of the functions for the two end members, i.e. CMS00.50 and CMS50.00 samples [Cormier *et al.*, 2010, Cormier and Cuello, 2012].

$F^N(Q)$ functions vary mainly between 4–12 Å⁻¹ while oscillations are very similar above 12 Å⁻¹. This

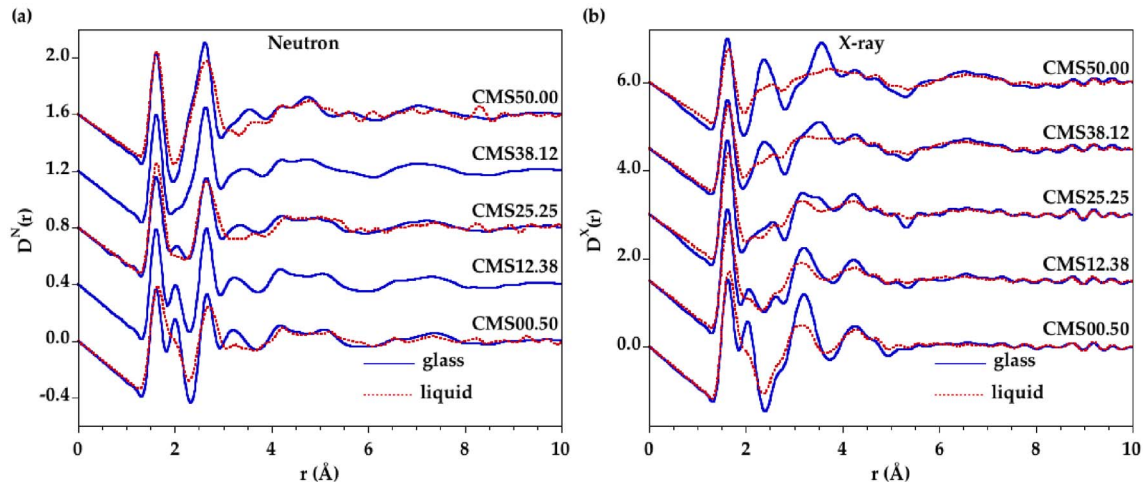


Figure 2. Comparison of the total pair distribution functions for the glasses and melts for (a) neutron and (b) X-ray diffraction. The blue solid curve corresponds to the glass and the dashed red curve is related to the liquid. Fourier transforms were obtained from the structure factors in Figure 1 with no modification function and using the range $0.56 \text{ \AA}^{-1} \leq Q \leq 22 \text{ \AA}^{-1}$.

latter region is mainly dominated by SRO associated with the silicate network. In the liquid state, the differences between samples are observed on a limited Q -region $3\text{--}7 \text{ \AA}^{-1}$. The differences with temperature reflect essentially increased degree of structural disorder. Above 7 \AA^{-1} , structure factors are not importantly changed because SRO remains very similar in glasses and liquids. At low Q values, broadening of the signal features is apparent in the liquid state.

The wollastonite compositions CMS50.00 have previously been studied in detail in the molten state using neutron and XRD techniques in combination with MD simulations [Benmore *et al.*, 2010, Skinner *et al.*, 2012]. Our ND data have better statistics, allowing more confidence at high Q -values. The Q_p peak has a higher intensity compared to Skinner *et al.* [Skinner *et al.*, 2012], which is in better agreement with room temperature data. The $F^X(Q)$ functions for the CMS50.00 glass and liquid are similar to those measured by Benmore *et al.* [2010], indicating reduced CaO evaporation during measurements. CMS00.50 has also been previously studied in the liquid state by Wilding *et al.* [Wilding *et al.*, 2010, 2008] and their XRD data are similar to those in the present study.

4.2. Real-space functions

The Fourier transformation of the total structure factor gives the corresponding real-space function (Figure 2), called total PDF $D(r)$. The first three major peaks in $D(r)$ are well understood and correspond to Si–O (1.62 Å), Mg–O (2.00 Å) and Ca–O (2.40 Å) correlations. Each radiation has a different sensitivity to the elements: XRD data are dominated by elements with high atomic number ($O < Mg < Si < Ca$) while ND data are dominated by elements with a high neutron scattering length, b , evolving as $b_{\text{Si}} = 4.153 \text{ fm} < b_{\text{Ca}} = 4.76 \text{ fm} < b_{\text{Mg}} = 5.37 \text{ fm} < b_{\text{O}} = 5.803 \text{ fm}$. These different sensitivities explain that the Ca–O correlation is clearly distinguished at 2.38 Å in $D^X(r)$ functions while they appear in $D^N(r)$ functions as a small hump on the low- r side of the peak at 2.63 Å that is dominated by O–O contributions. The presence of isobestic points can also be observed in the $D(r)$ functions (Supplementary Figure S2).

Variations at medium range distances are mainly associated with the silicate network in $D^N(r)$ functions and with correlations involving cations in $D^X(r)$ functions. In XRD data, the peak attribution has previously indicated that contributions near 3.16 Å are mainly due to Si–Mg and Mg–Mg correlations and contributions near 3.56 Å are mainly due to Ca–Ca and Ca–Si correlations [Cormier and Cuello,

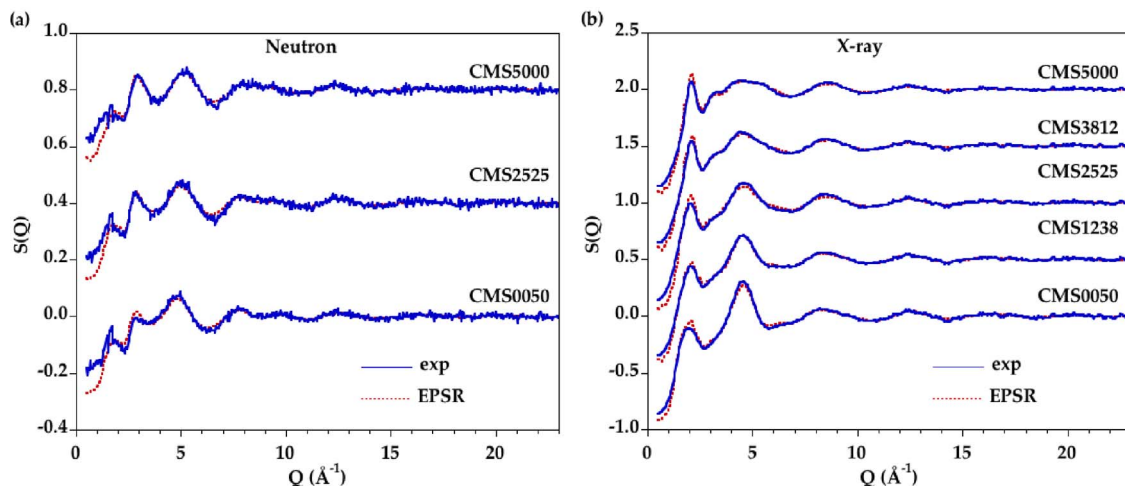


Figure 3. (a) Neutron and (b) X-ray experimental (blue line) and modeled (red dashed line) structure factors for CMS glasses.

2012]. The functions for all liquids have similar SRO compared to glasses, with a distinct Si–O contribution that is slightly shifted from 1.62 Å to 1.63 Å with temperature. However, the Mg–O and Ca–O peaks are no longer resolved indicating important thermal disordering due to broad distributions of Mg–O and Ca–O distances. In the liquids, the Mg–O peak overlaps with the Si–O one and the Ca–O peak is less resolved in the XRD data. The structural peaks in the $D^X(r)$ functions are clearly less resolved than in $D^N(r)$ functions at high temperature and the broadening of the peaks in $D^X(r)$ functions is increasing as the CaO content is increased.

4.3. EPSR models

Accurate information about the cation–oxygen local environment is difficult to obtain from direct analysis, for instance from Gaussian fits, due to large overlap between the various contributions, which is even enhanced as the temperature is increased. EPSR modelling is an alternative fitting method allowing the extraction of detailed structural information from atomic configurations. A good agreement is obtained by fitting simultaneously the neutron and XRD data, as seen in Figure 3 for all glasses and in Figure 4 for all liquids. The corresponding $D(r)$ functions are in Supplementary Figures S3 and S4. The reliability factors R_χ are determined on the $D(r)$ functions following Wright [Wright, 1993] and the values are reported

in Table 3. A good level of agreement between the EPSR models and the experimental data is achieved with R_χ factors comparable or better than published in previous studies [Gong *et al.*, 2021, Guignard and Cormier, 2008].

The EPSR-derived partial pair distribution functions (PPDFs) are shown in Figure 5 only for CMS00.50, CMS25.25 and CMS50.00 for clarity (all PPDFs for each glass/melt are in Supplementary Figure S5). The first peak in the Mg–O and Ca–O PPDFs exhibits a considerable broadening in the liquid state indicating that the oxygen disorder increases around these cations with temperature.

Using the minimum after the first main peak in Si–O, Mg–O and Ca–O PPDFs as a cutoff distance, the number of O neighbors around Si, Mg and Ca were determined. Cutoff distances are reported in Table 4. The average coordination numbers (CNs) are plotted in Figure 6. Silicon is mainly four-fold coordinated in all compositions for all glasses and liquids. Small amounts of three and five-coordinated Si sites (<3%) are observed and their proportion does not change significantly with composition or temperature. This is consistent with a corner-sharing tetrahedral silicate network dominating the liquid structure at ambient pressure. The CN(Mg–O) is around 4.5 in glasses and increases by ~ 0.25 with temperature. Similarly the CN(Ca–O) increases from ~ 5.8 in glasses to ~ 6.3 in liquids. However the CN as a function of r , $CN(r)$ (Figure 7), shows that defin-

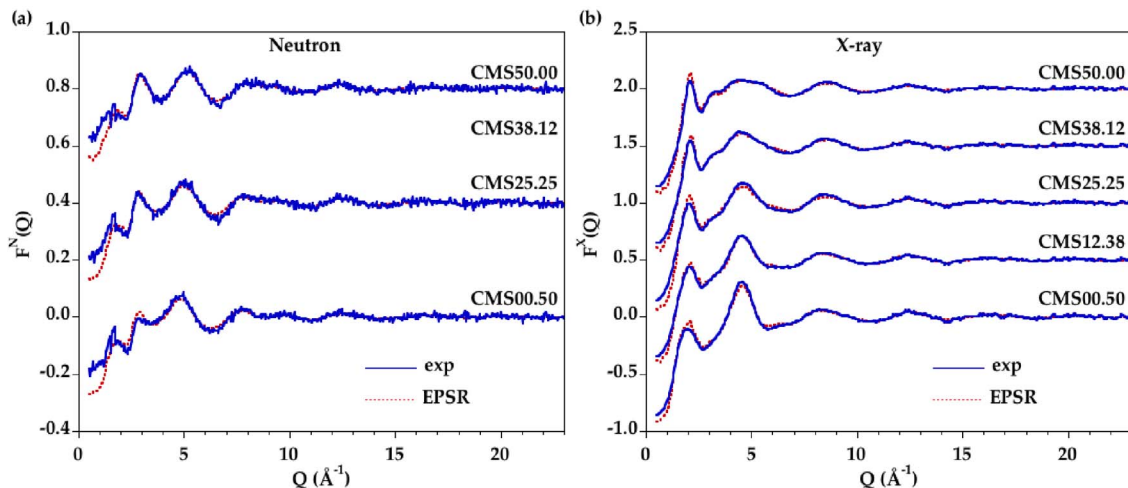


Figure 4. (a) Neutron and (b) X-ray experimental (blue curve) and modeled (red dashed curve) structure factors for CMS liquids.

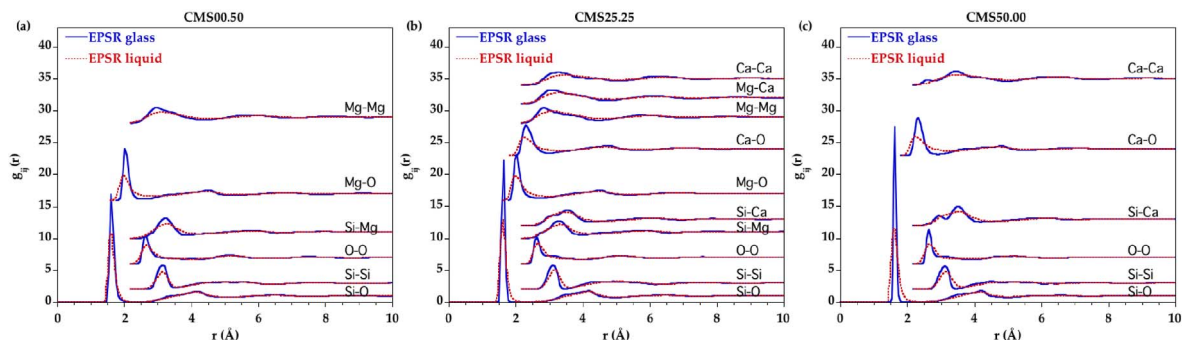


Figure 5. Comparison of the EPSR partial distribution functions for the glass (blue curve) and the liquid (red dashed curve) corresponding to the samples (a) CMS00.50, (b) CMS25.25 and (c) CMS50.00.

ing a cutoff distance in the liquid state is difficult since no clear plateau is apparent for Mg and Ca, contrary to Si. Therefore, defining the first shell of oxygen neighbors around Mg and Ca in the liquid state is non-ambiguous. This is due to the continuous distribution of Mg–O and Ca–O distances as revealed by the lack of minima going to zero in the Mg–O and Ca–O PPDFs.

The site distribution for Mg and Ca in glasses and liquids is provided in Figure 8, using the cutoff distances in Table 4. The x -fold sites are denoted $^{[x]}$ Mg or $^{[x]}$ Ca. In glasses, the site distribution indicates a majority of $^{[4]}$ Mg sites, with some $^{[5]}$ Mg sites, and a majority of $^{[6]}$ Ca sites with the coexistence of $^{[5]}$ Ca and $^{[7]}$ Ca sites. The Ca and Mg site distributions show

Table 4. Cutoff distances used in the calculation of average coordination numbers

	Si–O (Å)	Mg–O (Å)	Ca–O (Å)
Glass	2.10	2.60	2.95
Liquid	2.15	2.9	3.28

close similarities with previous models obtained by coupling MD and RMC (see Supplementary Figure S6) [Cormier and Cuello, 2012, 2011].

The distributions of bridging oxygens (BO), non-bridging oxygens (NBO) and free-oxygens (FO) (FO are not bonded to any Si atoms) are plotted in Figure 9a. The NBO fraction has a decreasing trend

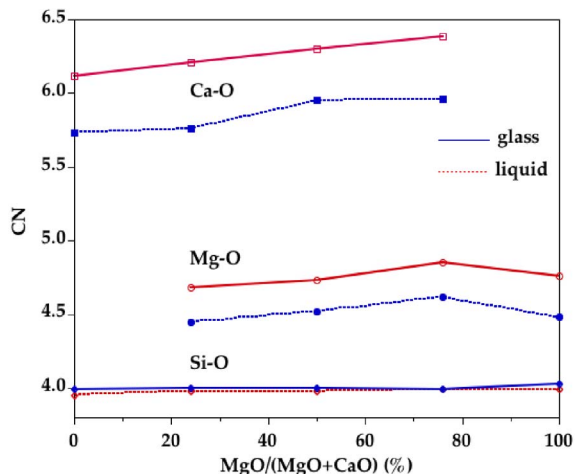


Figure 6. Composition dependence of the Si-O, Mg-O and Ca-O coordination numbers determined from EPSR models for glasses (blue curves) and liquids (red dashed curves).

with increasing MgO content. The presence of triply bonded O is always less than 0.9% of all oxygen atoms in glasses/liquids and the content is thus not significant. In the liquid state, the NBO proportion increases, which is concomitant with a decrease in BO and FO. The low BO proportion is reflected by a lower average network connectivity that is quantified by the average number of n BO atoms around a silicon atom (Figure 9b). The average network connectivity shows increasing values as the MgO content increases in glasses and liquids.

5. Discussion

5.1. Comparison between atomistic models

The EPSR models can be compared to our previous results obtained by combining MD simulations with RMC modelling [Cormier and Cuello, 2012]. In CMS00.50, the average CN for Mg remains similar: $CN_{MD+RMC} = 4.35$ and $CN_{EPSR} = 4.48$ (Supplementary Figure S6a,b). The distribution of the various coordination sites gives almost an equal amount of $^{[4]}Mg$ (52%) and $^{[5]}Mg$ (41%) in EPSR while $^{[4]}Mg$ was predominant (68%) in the MD+RMC model. For Ca in CMS50.00, the average CN and the site distribution are not substantially changed (Supplementary Figure

S6c,d). It thus appears that both methods of data fitting give convergent results, strengthening the validity of this approach to determine the SRO.

The distributions of BO, NBO and FO show that EPSR models contain more BO and free O compared to MD+RMC models, with a slight compositional dependence (Figure 9a). The higher BO content explains a high average connectivity in EPSR models (Figure 9b) that increases with the MgO content as in MD+RMC models. The $MgSiO_3$ - $CaSiO_3$ join corresponds to metasilicate compositions so that n is expected to have a value of 2. The departure from this value for glasses is higher for EPSR than for MD+RMC. Interestingly, the liquid EPSR models have values closer to MD+RMC models, probably because MD+RMC models retain more structural characteristic features of the high-temperature state due to the intrinsic fast quenching rates in MD simulations and insufficient relaxation of the structure in RMC modelling of glasses.

The Q^n speciation (Q^n is a SiO_4 tetrahedra containing n BO atoms) shows more Q^3 and Q^4 and less Q^2 , Q^1 and Q^0 in EPSR models compared to MD+RMC models (Figure 10). Both models present discrepancies with the Q^n proportions determined experimentally by ^{29}Si NMR for CMS00.50, CMS25.25 and CMS50.00 glasses [Schneider *et al.*, 2003, Sen *et al.*, 2009, Zhang *et al.*, 1997], as these measurements determined higher Q^2 and Q^1 contents and lower Q^3 and Q^4 contents compared to models. A recent MD study with advanced potentials indicates Q^n speciation for CMS00.50 and CMS50.00 very similar to our results with an underestimation of Q^2 and an overestimation of Q^3 and Q^4 [Shih *et al.*, 2021]. These results indicate that additional constraints should be incorporated in the models to improve the description of some specific structural units or groups. Moreover, careful comparison between experimental and atomistic models should be provided to ensure continuous improving in modelling and simulations of glasses and melts.

5.2. Evolution of Si environment with temperature

For the Si-O pair, the $CN(r)$ shows a clear plateau (Figure 7a) that indicates a well-defined environment around Si atoms corresponding to SiO_4 tetrahedra in both glasses and liquids, with very small proportions

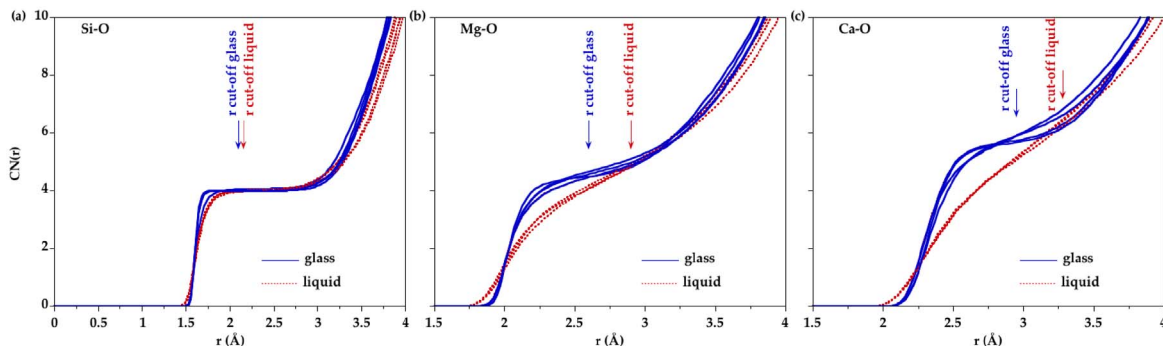


Figure 7. Evolution of coordination number with cutoff distance for (a) Si–O, (b) Mg–O and (c) Ca–O pairs as determined from EPSR models.

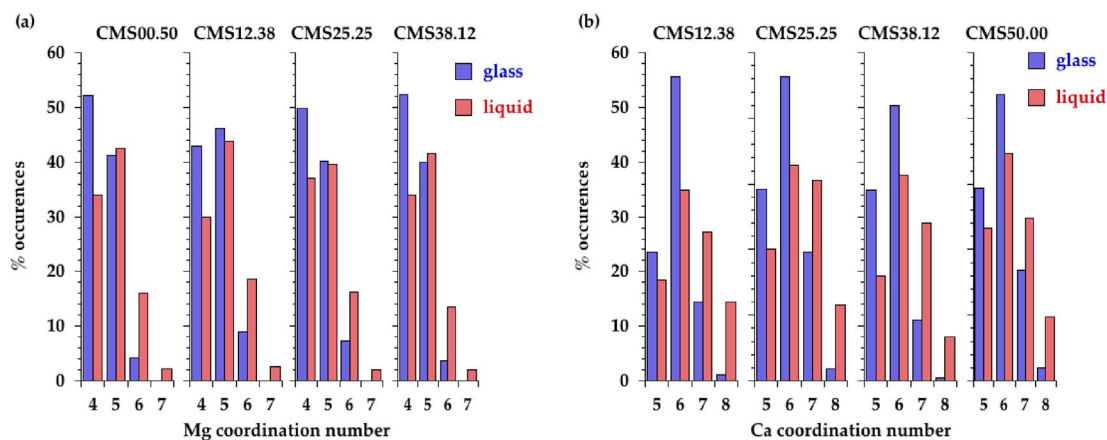


Figure 8. Distribution of (a) Mg and (b) Ca polyhedra extracted from EPSR models in the different glasses and melts.

of other coordinated sites. SiO_4 tetrahedra are poorly affected by an increase in temperature. The position of the first peak in the total $D(r)$ functions is not informative as it is affected by Mg–O contributions. In CMS50.00 (Mg-free sample), the position of the Si–O peak is increased by $+0.01 \text{ \AA}$ with temperature. The Si–O PPDFs determined from the EPSR models do not show significant changes with temperature except a broadening consistent with thermal disordering.

The structure along the MgSiO_3 – CaSiO_3 join is highly depolymerized with a high proportion of Q^2 and Q^3 species, in agreement with previous experimental findings [De Sousa Meneses *et al.*, 2006, Schneider *et al.*, 2003, Zhang *et al.*, 1997]. However, the degree of connectivity displayed in Figure 9b is higher than expected considering the stoichiome-

try. The glass/melt structures present a broad range of Q^n species compared to the structure of crystalline counterparts that is composed only of Q^2 species. Based on observations on the 3D configurational boxes, the silicate network may possibly be described as a chain-like network structure of corner-sharing SiO_4 tetrahedra forming broken chains coexisting with few rings. This differs from the topology of pyroxenes and pyroxenoids that is composed only of tetrahedral chains. Moreover, chemical evolutions are visible in Figure 9: the substitution of Ca by Mg yields a slight increase in connectivity associated with more BO and FO. However, as Mg and Ca cations have the same charge, the Mg/Ca mixing does not require significant charge redistribution in the structure, which explains small network modifications (Figures 9 and 10). The difference in cationic

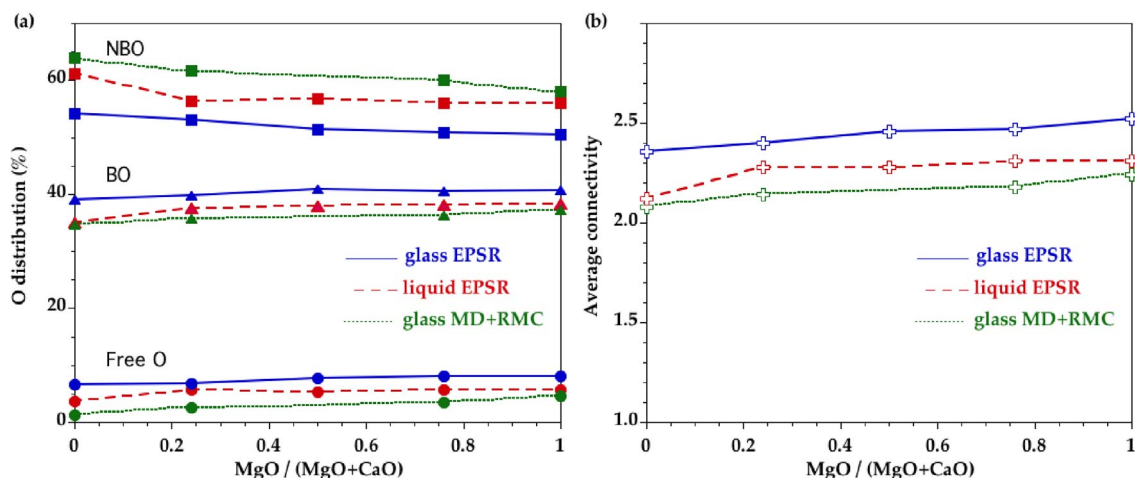


Figure 9. (a) Oxygen distribution between non-bridging oxygen (NBO, squares), bridging oxygen (BO, triangles) and free oxygen (free O, circles), calculated from the EPSR models for CMS glasses (plain curves) and melts (long dashed curves). Comparison is made with previous glass models obtained by combining MD and RMC (short dashed curves) [Cormier and Cuello, 2012]. Lines are only to guide the eye. (b) Average connectivity, n , derived from the EPSR models for the CMS glasses (plain curve) and melts (long dashed curve). Comparison is made with previous glass models obtained by combining MD and RMC (short dashed curve) [Cormier and Cuello, 2012]. Lines are only to guide the eye.

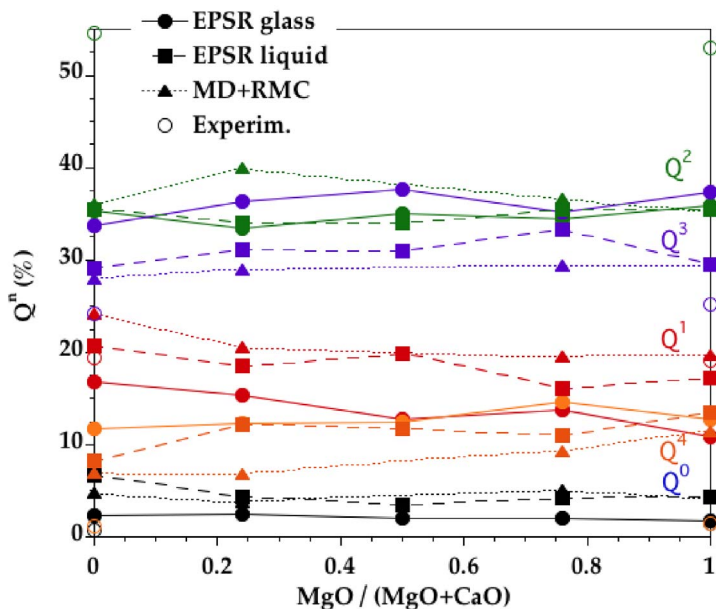


Figure 10. Q^n distribution derived from the EPSR models for the CMS glasses (circles, plain curves) and liquids (squares, long dashed curves). Comparison is made with previous glass models obtained by combining MD and RMC (triangles, short dashed curves) [Cormier and Cuello, 2012] and experimental point (open symbols) [Schneider *et al.*, 2003, Sen *et al.*, 2009, Zhang *et al.*, 1997]. Lines are only to guide the eye.

radii is essentially accommodated by a distribution of the two cations in multiple distinct sites (Figures 7 and 8).

There is a clear trend for higher NBO content and lower BO and FO contents in liquids compared to glasses (Figure 9a). These changes in oxygen speciation, associated with lower Q^3 species and higher Q^1 species, indicate that the liquid network is less connected. FO species correspond to oxygen not bounded to any SiO_4 tetrahedra and can thus be a signature for regions that are enriched in Mg and Ca. Conversely, the high proportion of BO can indicate highly polymerized silicate regions depleted in Mg and Ca. As FO and BO contents increase upon cooling, the segregation between silicate-rich and (Mg,Ca)-rich regions is more important in glasses compared to melts.

5.3. Evolution of Mg environment with temperature

In glasses, the Mg site distribution indicates not only a prevalence of $^{[4]}\text{Mg}$ sites but also a large amount of $^{[5]}\text{Mg}$ sites. The presence of polyhedra with 4- and 5-fold coordination is also well established for other divalent cations such as Fe^{2+} , Ni^{2+} or Zn^{2+} [Cormier *et al.*, 2021, Galois and Calas, 1993, Jackson *et al.*, 2005, Waychunas *et al.*, 1988]. In the liquids, higher coordinated sites are present, mainly $^{[5]}\text{Mg}$ and a small amount of $^{[6]}\text{Mg}$, coexisting with still a large amount of $^{[4]}\text{Mg}$ (Figure 8). Upon increasing temperature, there is thus a site redistribution that is reflected in the evolution of the average $\text{CN}(\text{Mg-O})$ near 4.5 in glasses and near 4.7–4.8 in liquids. These values agree with very recent MD simulations for CMS00.50 [Shih *et al.*, 2021]. The Mg–O environment is more ordered in CMS00.50 glass compared to other glasses as seen in the Mg–O PPDF that exhibits a well-defined first peak (Figure 5a). The average $\text{CN}(\text{Mg-O})$ in CMS00.50 is the lowest, in agreement with previous findings [Cormier and Cuello, 2012]. Otherwise there is no clear compositional dependence either in glasses or in liquids within the scatter of the data. A plateau is discernible in the $\text{CN}(r)$ in glasses (Figure 7b), allowing to define the first oxygen coordination shell around Mg atoms, whereas it is more difficult to determine the correct inflexion points for liquids. Inspection of the first peak position in the Mg–O PPDFs reveals a shift from $2.02 \pm 0.02 \text{ \AA}$ in glasses

to $1.98 \pm 0.02 \text{ \AA}$ in liquids (Figure 5 and Supplementary Figure S7a). Though this evolution of the maximum peak position could indicate a coordination decrease, a long tail in the high r -side in liquids implies the contribution of additional long Mg–O distances that explain the increase in CN with temperature. Previous XRD or EXAFS studies have usually obtained low Mg CNs [Matsubara *et al.*, 1988, Taniguchi *et al.*, 1997, Yin *et al.*, 1983] due to the difficulties to correctly determine the CN when an asymmetric distribution of distances exists. Because of disorder and site distortion, high- r contributions are regularly not detected in EXAFS data as this method is more sensitive to nearest neighbors [Kroeker and Stebbins, 2000]. The modelling approaches (EPSR or RMC) give a more accurate determination of CN as this value is not based on a Gaussian fit.

The shortening of Mg–O distances in the liquids is remarkable since a thermal expansion is expected. These short Mg–O distances are compensated by the presence of long Mg–O ones, resulting in the high r -side tail and yielding a more distorted environment in the liquid than in the glass. A different behavior may be observed for divalent transition metals in the molten states. Indeed, a shortening of the Ni–O distances in a $\text{Na}_{1.95}\text{Ni}_{0.05}\text{Si}_2\text{O}_5$ melt has been inferred by high-temperature X-ray absorption spectroscopy [Farges *et al.*, 1994]. This was interpreted as an increasing content of $^{[4]}\text{Ni}$ during the glass to melt transition. Fe^{2+} has also been found in four-fold coordination in alkali silicate glasses and melts with no temperature effects [Waychunas *et al.*, 1988]. However such EXAFS studies may be insensitive to long Ni–O or Fe–O distances, especially in the liquid state.

Very few studies have been performed *in situ* to understand the Mg environment in silicate melts. George and Stebbins have obtained ^{25}Mg NMR spectra up to 1743 K in a diopside melt and a melt close to CMS12.38 compositions (but with 6 mol% Al_2O_3) [George and Stebbins, 1998] and Fiske and Georges on CMS29.14 at 1673 K [Fiske and Stebbins, 1994]. For the liquids, George and Stebbins have observed a change with addition of Ca (or alkalis) with a shift of the peak position to higher frequencies indicating a decrease in the average $\text{CN}(\text{Mg-O})$. However these changes are small. There is a strong temperature dependence of $\text{CN}(\text{Mg-O})$ with substantially smaller CN in the glass [Fiske and Steb-

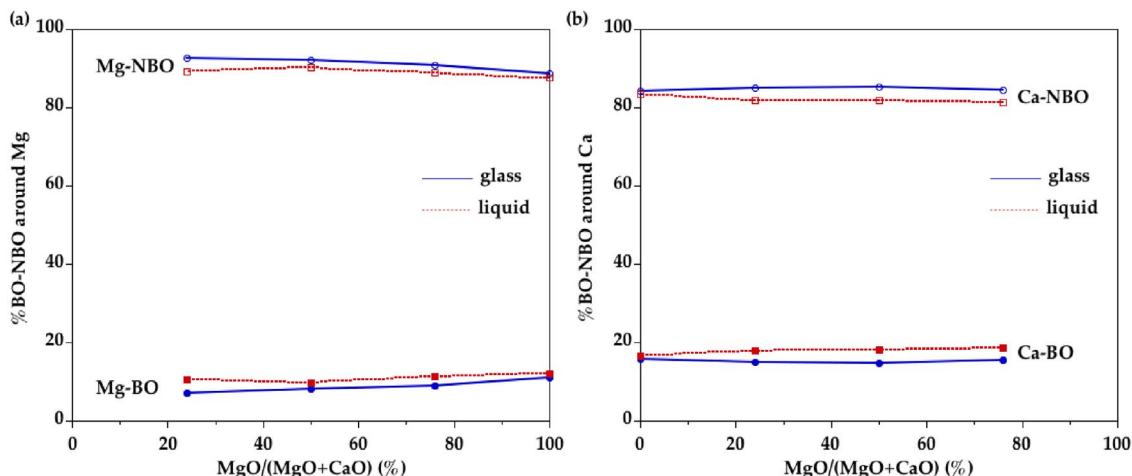


Figure 11. Proportion of NBO and BO neighbors around (a) Mg and (b) Ca, as determined in the first shell of O neighbors in EPSR models of glasses and liquids.

bins, 1994]. The NMR chemical shifts at high temperatures are in agreement with a CN between five and six and significantly different to the one expected for four-fold coordination [George and Stebbins, 1998]. This behavior is consistent with the increase in CN from the glass to the liquid as deduced from the present diffraction data analysis. Gaussian fits of high-temperature X-ray PDF do not show any Mg coordination change for the enstatite composition (CMS00.50) [Wilding *et al.*, 2010], while a small Mg–O coordination increase from 4.8 in the glass to 5.1 in the liquid for a CMS37.00 sample (37.5MgO–62.5SiO₂) has been revealed using several Gaussian functions to fit the Mg–O contribution [Benmore *et al.*, 2020].

5.4. Evolution of Ca environment with temperature

Similar to Mg, analysis of EPSR models indicate that Ca cations are localized in a wide distribution of sites (Figure 8b). The Ca environment is dominantly ⁶Ca with both ⁵Ca and ⁷Ca in glasses. The site speciation is redistributed to higher coordinated sites in liquids (Figure 8b): less ⁵Ca and ⁶Ca and more ⁷Ca and ⁸Ca. The average coordination of Ca is higher than that of Mg in agreement with its lower field strength (defined as the ratio z/d^2 , where z denotes the cation charge and d is the cation–oxygen bond length). Evolution of the first Ca–O distance in the

Ca–O PPDFs shows a similar behavior than the Mg–O ones with increasing temperature: shortening of the average Ca–O bond length from 2.30 ± 0.02 Å to 2.25 ± 0.01 Å and a broadening and asymmetric distribution to the high r -side (Figure 5 and Supplementary Figure S7b). The average CN(Ca–O) is increased from ~ 5.8 in the glasses to ~ 6.3 in the liquids. This is consistent with MD simulations of CaSiO₃ glass/melt that indicate both short and long Ca–O distances in the melt [Skinner *et al.*, 2012]. In the latter investigation, a symmetric Gaussian fit of the first Ca–O peak yields a decrease in the Ca–O CN from 6 in the glass to 5 in the liquid [Skinner *et al.*, 2012]. However, using additional Gaussian functions in the fit, the CN(Ca–O) does not vary with temperature (6.6 in the glass and 6.5 in the liquid) for a CMS20.00 sample (20CaO–80SiO₂) measured using high-temperature XRD [Benmore *et al.*, 2020]. This again emphasizes that a distorted environment cannot easily be captured by a simple Gaussian fit.

5.5. Distribution of Ca and Mg

To understand the connection of Mg sites with the tetrahedral silicate network, we have calculated the number of NBO and BO around cations (Figure 11). An important proportion of O neighbors are NBO ($\sim 60\%$) and this proportion decreases only weakly with temperature. The proportion of BO in the first coordination shell around Ca is higher than for Mg

indicating a preferential association of Ca with BO. This is attributed to the lower field strength of Ca compared to Mg and thus its lower ability to charge-balance the negative charge around NBO sites. A ^{41}Mg site implies strong bond strengths and, thereby, a BO atom that is connected to two SiO_4 and one MgO_4 would be severely overbonded. Therefore, the oxygen connecting Mg to Si is preferentially a NBO atom. The high proportion of Ca–BO bonds may be explained by Ca atoms partly residing in more polymerized silicate-rich regions. This different behavior between Mg and Ca is supported by a O^{17} -NMR study indicating that the Ca–Mg cation mixing may not be entirely random along the MgSiO_3 – CaSiO_3 join [Allwardt and Stebbins, 2004]. However, the Ca–Mg ordering is small compared to other cation mixing that associates cations having larger differences in charge and radius [Cormier *et al.*, 2010]. The increase in Ca and Mg CNs in the liquids is associated with higher proportions of BO in the first coordination shell but the preferential association of BO around Ca is preserved.

The connection of cations with the silicate network can be further probed from the Si–Mg and Si–Ca PPDFs (Figure 5 and Supplementary Figure S7c,d). In the Si–Mg PPDFs, the first peak is at 3.2 Å in glasses and at 3.3 Å in liquids. The shift is small but apparent (Supplementary Figure S7c). These distances determined from the EPSR fits mainly indicate corner-sharing polyhedra. Indeed, very few examples of edge-sharing between MgO_4 and SiO_4 in EPSR models give Si–Mg distances at 2.7–2.9 Å. In the Mg–Si PPDFs in Figure 12a (see also Supplementary Figure S8a), a shoulder at 2.75 Å is discernible in the first peak at 3.28 Å and correspond to edge-sharing between SiO_4 tetrahedra and ^{51}Mg and ^{61}Mg sites. This is also consistent with a recent DFT numerical study of Ca–Mg aluminosilicate glasses [Gong *et al.*, 2021]. The intensity at the position of edge-sharing is higher in liquids while the corner-sharing intensity dominates in glasses. Similarly in Mg–Mg PPDFs (Figure 12c and Supplementary Figure S8c), the intensity at edge-sharing position between Mg polyhedra is higher in glasses than in liquids, and this latter shows higher intensities at Mg–Mg face-sharing and corner-sharing positions. This variation in Mg–Si and Mg–Mg PPDFs indicate less variability in glasses compared to liquids with mainly Mg–Si corner-sharing and Mg–Mg edge-sharing at ambient

temperature.

Two distinct peaks are observed in the Ca–Si PPDF of glasses (Figure 12b and Supplementary Figure S8b) at 2.95 Å and 3.50 Å that are assigned to edge- and corner-sharing connectivity between SiO_4 tetrahedra and Ca polyhedra, respectively [Gong *et al.*, 2021], with dominantly corner-sharing linkages. The intensity corresponding to Si–Ca edge-sharing decrease with temperature, a behavior dissimilar to Si–Mg linkages. The Ca–Ca PPDFs show a small peak at 2.60 Å that decreases with less CaO content, indicating a significant proportion of Ca–Ca face-sharing in CMS50.00 glass (Figure 12e and Supplementary Figure S8e). Such face-sharing connections are characteristic features of Ca-rich glasses as they disappear in the corresponding liquids. The large fraction of Ca–Ca face-sharing in the glass suggests nano-heterogeneities and Ca clustering [Benmore *et al.*, 2010], which can result from partial liquid–liquid phase separation upon cooling [Benmore *et al.*, 2020].

Upon cooling, a decrease in the population of Ca–Ca corner-sharing and an increase in Ca–Ca edge-sharing were previously suggested based on analysis of bond angle distributions in MD simulations of CaSiO_3 glass/melt [Benmore *et al.*, 2010]. This result is confirmed in the present investigation based on PPDFs analysis in all glasses and this trend is observed for both Ca–Ca and Ca–Mg linkages (Ca–Mg corner-sharing position has lower intensities and Ca–Mg edge-sharing position has higher intensities with a temperature decrease). For the intermediate compositions, the Ca–Mg contribution (Figure 12d) is well-defined, in agreement with a mixing between the two different cations.

The increasing fraction of edge-shared Ca/Mg polyhedra with decreasing temperature results in increasing the polymerization and Ca/Mg clustering. The Ca/Mg aggregation increases more rapidly near the glass transition temperature, which can partly explain the steep continuous rise in viscosity in the supercooled liquid as T_g is approached [Benmore *et al.*, 2010, Skinner *et al.*, 2012].

5.6. Structure of silicate melts

Glasses differ from melts by the configurational contributions that appear in thermodynamic properties above T_g and that imply a substantial change in

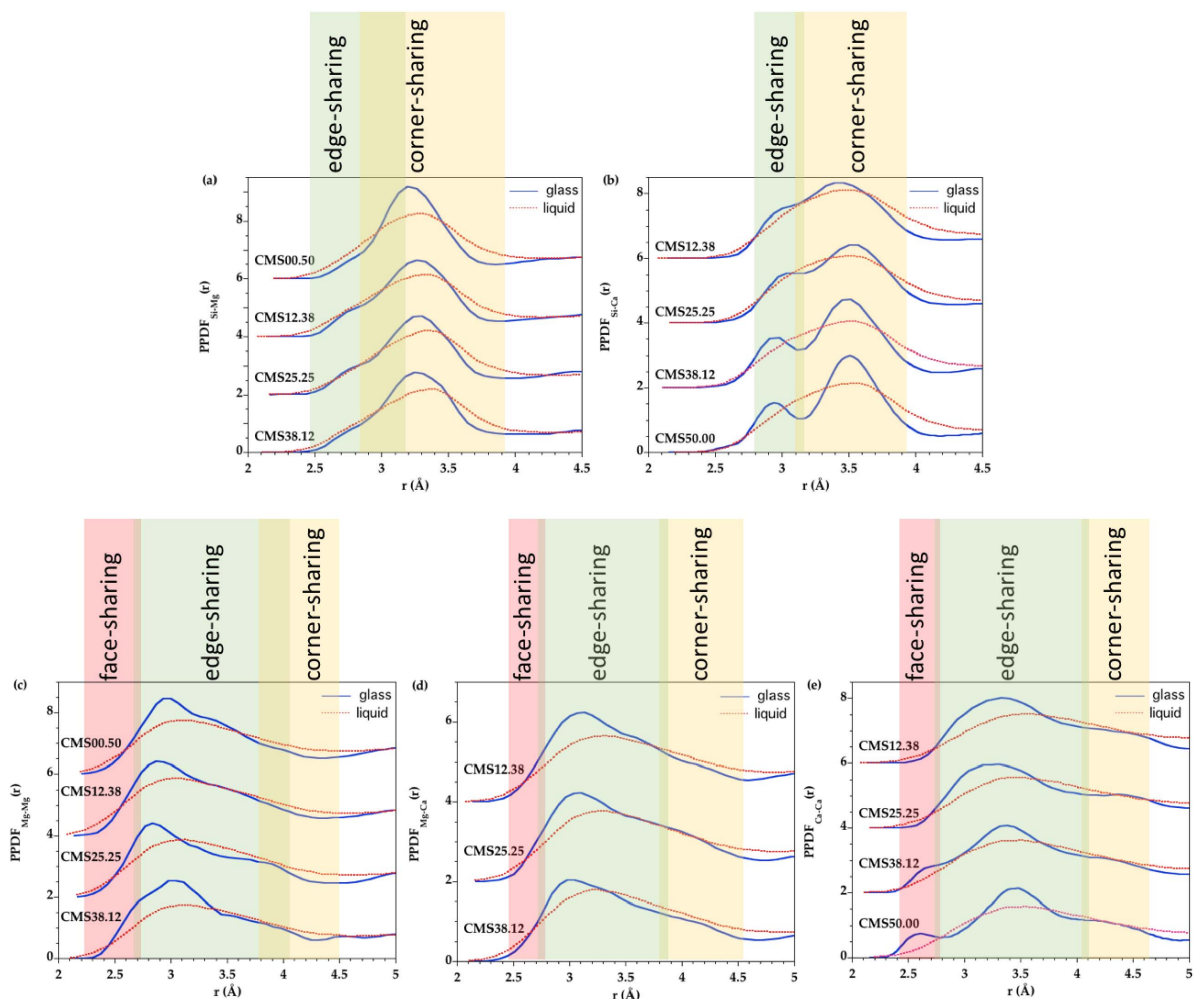


Figure 12. EPSR partial pair distribution functions for the glass (blue curve) and the liquid (red dashed curve) for the different samples, highlighting the bond length regions characteristics of face-, edge- and corner-sharing for (a) Si–Mg, (b) Si–Ca, (c) Mg–Mg, (d) Mg–Ca and (e) Ca–Ca pairs.

structure with temperature. In silicate glasses/melts, a change in Q^n distribution has been inferred from Raman and NMR studies, indicating that the disproportionation reaction $2Q^n \rightleftharpoons Q^{n-1} + Q^{n+1}$ is displaced to the right in melts [Mysen and Frantz, 1993, Stebbins, 1995]. Though this contribution is important, the resulting heat capacity cannot account completely for the measured configurational heat capacity, indicating the occurrence of other structural modifications [Stebbins, 2008]. In the EPSR models, changes in Q^n distribution is small (less Q^3 and more Q^1 and Q^0 at high temperature). Additional

temperature-induced structural changes can be various: conformational relaxation of the network at IRO, site thermal expansion, coordination change or local distortion [Calas *et al.*, 2006, Henderson *et al.*, 2006, Majérus *et al.*, 2004]. For the CMS system, the present analysis points to a considerable disordering around Mg and Ca cations at both short and medium range scale, as both cations in melts tend to enter larger sites with a change in the connection between polyhedra (Figures 8 and 12). The enhanced cation mobility with temperature allows cations to explore energetically less favorable sites with higher coordina-

tion that favors an entropy increase [de Ligny and Westrum, 1996].

Our results indicate that the glass/melt structures of the two end members present significant differences though the well-defined Mg–Ca PPDFs is indicative of substantial mixing between the two sub-structures. The average CN is different between Mg and Ca with high coordinated sites for Ca and the increase in temperature yields the cations to be localized in further more coordinated sites. As a likely consequence of the larger cationic polyhedra, major modifications with temperature are seen in the cation–cation or cation–silicon linkages to accommodate the random packing of distinct MgO_x and CaO_x polyhedra. The greater diversity of connections explains an increase of the configurational entropy in the liquids. The structural organization evolves continuously with compositions between the two end members and, thereby, the changes are compatible with the expected ideal Ca/Mg mixing [Neuville and Richet, 1991].

Dynamic processes such as viscous flow are controlled by the mechanism of Si–O bond breaking occurring during Q^n -species exchange, as proposed for SiO_2 -rich silicate liquids [Farnan and Stebbins, 1994]. In more depolymerized liquids, it was suggested that Ca–O and Mg–O bond breaking and cation mobility could significantly participate to structural relaxation and flow processes [Nasikas *et al.*, 2012]. Indeed, a correlation between Mg motions and viscosity was confirmed in a high-temperature NMR study [George and Stebbins, 1998], which indicates that this cation is strongly bounded to the silicate network. The cationic dynamics could be further enhanced by the increase entropy in the liquids resulting from diverse MgO_x and CaO_x connections. No studies have investigated in details the relaxation near T_g and it is then an open question if a decoupling behavior occurs as in aluminosilicate systems [Gruener *et al.*, 2001] and if there is a different decoupling behavior between Mg and Ca containing systems.

When approaching the glass transition, it has been demonstrated that CaO_x edge-shared polyhedra tend to cluster within the silicate network of CaSiO_3 [Benmore *et al.*, 2010, Skinner *et al.*, 2012]. Similar increasing cationic heterogeneities are suggested in the present study for the complete MgSiO_3 – CaSiO_3 join. The increase in IRO near T_g precludes the liquid to

find a minimum basin corresponding to the crystal structure in its potential energy landscape. Such heterogeneities related to the Mg/Ca organization could also limit cation mobility, increase the viscosity and thereby favor glass formation. The presence of intrinsic heterogeneities in the glass structure has been reported recently in many aluminosilicate systems for cation mixing (Na–K aluminosilicate [Le Losq *et al.*, 2017, Le Losq and Neuville, 2013]; Ca–Mg aluminosilicate [Allu *et al.*, 2018] and their spatial extent can be affected by the quenching rate [Dargaud *et al.*, 2012].

6. Conclusions

The structure of a series of CaSiO_3 – MgSiO_3 glasses and melts have been investigated by neutron and XRD using aerodynamic levitation. Experimental data have been fitted using the EPSR method to obtain atomistic models over the short and medium range order. The coordination of Mg and Ca has been determined at ambient and high temperature. Results show sites with higher coordination in the liquids compared to those in the glasses. This CN evolution implies modifications of the connection between Ca and Mg polyhedra and the connection of Ca and Mg polyhedra with SiO_4 tetrahedra. Specifically, decreasing the temperature increases the proportion of Si–(Mg,Ca) corner-sharing, Si–Ca edge-sharing, (Mg,Ca)–(Mg,Ca) face- and edge-sharing and decreases the proportion of (Mg,Ca)–(Mg,Ca) corner-sharing. These changes suggest cationic heterogeneities along the glass series. Ca-rich compositions present Ca–Ca face-sharing and Ca is more connected to BO than Mg indicating that Ca^{2+} cations are slightly preferentially localized in polymerized silicate regions. The findings of these modifications at IRO bring a deeper understanding of the configurational changes with temperature.

Conflicts of interest

Authors have no conflict of interest to declare.

Supplementary data

Supporting information for this article is available on the journal's website under <https://doi.org/10.5802/crgeos.112> or from the author.

References

- Allu, A. R., Gaddam, A., Ganiseti, S., Balaji, S., Siegel, R., Mather, G. C., Fabian, M., Pascual, M. J., Ditaranto, N., Milius, W., Senker, J., Agarkov, D. A., Kharton, V. V., and Ferreira, J. M. F. (2018). Structure and crystallization of alkaline-earth aluminosilicate glasses: prevention of the alumina-avoidance principle. *J. Phys. Chem. B*, 122, 4737–4747.
- Allwardt, J. R. and Stebbins, J. F. (2004). Ca–Mg and K–Mg mixing around non-bridging O atoms in silicate glasses: an investigation using ^{17}O MAS and 3QMAS NMR. *Am. Mineral.*, 89, 777–784.
- Benmore, C. J., Alderman, O. L. G., Benmore, S. R., Wilke, S. K., and Weber, R. J. K. (2020). Small- and wide-angle X-ray scattering studies of liquid–liquid phase separation in silicate melts. *ACS Earth Space Chem.*, 4, 1888–1894.
- Benmore, C. J., Weber, J. K. R., Wilding, M. C., Du, J., and Parise, J. B. (2010). Temperature-dependent structural heterogeneity in calcium silicate liquids. *Phys. Rev. B*, 82, article no. 224202.
- Calas, G., Majerus, O., Galois, L., and Cormier, L. (2006). Crystal field spectroscopy of Cr^{3+} in glasses: compositional dependence and thermal site expansion. *Chem. Geol.*, 229, 218–226.
- Cormier, L. (2019). Neutron and X-ray diffraction of glass. In Musgraves, J. D., Hu, J., and Calvez, L., editors, *Springer Handbook of Glass*, pages 1047–1094. Springer International Publishing, Cham.
- Cormier, L., Calas, G., and Cuello, G. J. (2010). Structural study of Ca–Mg and K–Mg mixing in silicate glasses by neutron diffraction. *J. Non-Cryst. Solids*, 356, 2327–2331.
- Cormier, L., Calas, G., and Gaskell, P. H. (2001). Cationic environment in silicate glasses studied by neutron diffraction with isotopic substitution. *Chem. Geol.*, 174, 349–363.
- Cormier, L. and Cuello, G. J. (2011). Mg coordination in a MgSiO_3 glass using neutron diffraction coupled with isotopic substitution. *Phys. Rev. B*, 83, article no. 224204.
- Cormier, L. and Cuello, G. J. (2012). Structural investigation of glasses along the MgSiO_3 – CaSiO_3 join: diffraction studies. *Geochim. Cosmochim. Acta*, 122, 498–510.
- Cormier, L., Delbes, L., Baptiste, B., and Montouillout, V. (2021). Vitrification, crystallization behavior and structure of zinc aluminosilicate glasses. *J. Non-Cryst. Solids*, 555, article no. 120609.
- Courtial, P. and Dingwell, D. B. (1995). Nonlinear composition dependence of molar volume of melts in the CaO – Al_2O_3 – SiO_2 system. *Geochim. Cosmochim. Acta*, 59, 3685–3695.
- Courtial, P. and Dingwell, D. B. (1999). Densities of melts in the CaO – MgO – Al_2O_3 – SiO_2 system. *Am. Mineral.*, 84, 465–476.
- Cuello, G. J., Cristiglio, V., Hennem, L., and Puente-Orench, I. (2014). Neutron scattering at high temperature and levitation techniques. *J. Phys. Conf. Ser.*, 549, article no. 012002.
- Dargaud, O., Cormier, L., Menguy, N., and Patriarche, G. (2012). Multi-scale structuration of glasses: observations of phase separation and nanoscale heterogeneities in glasses by Z-contrast scanning electron transmission microscopy. *J. Non-Cryst. Solids*, 358, 1257–1262.
- de Ligny, D. and Westrum, E. F. (1996). Entropy of calcium and magnesium aluminosilicate glasses. *Chem. Geol.*, 128, 113–128.
- De Sousa Meneses, D., Malki, M., and Echegut, P. (2006). Optical and structural properties of calcium silicate glasses. *J. Non-Cryst. Solids*, 352, 5301–5308.
- Drewitt, J. W. E., Jahn, S., Cristiglio, V., Bytchkov, A., Leydier, M., Brassamin, S., Fischer, H. E., and Hennem, L. (2011). The structure of liquid calcium aluminates as investigated using neutron and high energy X-ray diffraction in combination with molecular dynamics simulation methods. *J. Phys. Condens. Matter*, 23, article no. 155101.
- Drewitt, J. W. E., Sanloup, C., Bytchkov, A., Brassamin, S., and Hennem, L. (2013). Structure of $(\text{Fe}_x\text{Ca}_{1-x}\text{O})_y(\text{SiO}_2)_{1-y}$ liquids and glasses from high-energy X-ray diffraction: implications for the structure of natural basaltic magmas. *Phys. Rev. B*, 87, article no. 224201.
- Farges, F., Brown, G. E., Calas, G., Galois, L., and Waychunas, G. A. (1994). Structural transformation in Ni-bearing $\text{Na}_2\text{Si}_2\text{O}_5$ glass and melt. *Geophys. Res. Lett.*, 21, 1931–1934.
- Farnan, I. and Stebbins, J. F. (1994). The nature of the glass transition in a silica-rich oxide melt. *Science*, 265, 1206–1209.
- Fiske, P. S. and Stebbins, J. F. (1994). The structural role of Mg in silicate liquids: a high-temperature ^{25}Mg , ^{23}Na , and ^{29}Si NMR study. *Am. Mineral.*, 79, 848–861.

- Galoisy, L. and Calas, G. (1993). Structural environment of nickel in silicate glass/melt systems: Part 1. Spectroscopic determination of coordination states. *Geochim. Cosmochim. Acta*, 57, 3613–3626.
- Gaskell, P. H., Eckersley, M. C., Barnes, A. C., and Chieux, P. (1991). Medium-range order in the cation distribution of a calcium silicate glass. *Nature*, 350, 675–677.
- George, A. M. and Stebbins, J. F. (1998). Structure and dynamics of magnesium in silicate melts; a high-temperature ^{25}Mg NMR study. *Am. Mineral.*, 83, 1022–1029.
- Gong, K., Özçelik, V. O., Yang, K., and White, C. E. (2021). Density functional modeling and total scattering analysis of the atomic structure of a quaternary $\text{CaO-MgO-Al}_2\text{O}_3\text{-SiO}_2$ (CMAS) glass: uncovering the local environment of calcium and magnesium. *Phys. Rev. Mater.*, 5, article no. 015603.
- Gruener, G., Odier, P., De Sousa Meneses, D., Florian, P., and Richet, P. (2001). Bulk and local dynamics in glass-forming liquids: a viscosity, electrical conductivity, and NMR study of aluminosilicate melts. *Phys. Rev. B*, 64, article no. 24206-1-5.
- Guignard, M. and Cormier, L. (2008). Environments of Mg and Al in $\text{MgO-Al}_2\text{O}_3\text{-SiO}_2$ glasses: a study coupling neutron and X-ray diffraction and reverse Monte Carlo modeling. *Chem. Geol.*, 256, 111–118.
- Henderson, G. S., Calas, G., and Stebbins, J. F. (2006). The structure of silicate glasses and melts. *Elements*, 2, 269–273.
- Hennet, L., Cristiglio, V., Kozaily, J., Pozdnyakova, I., Fischer, H. E., Bytchkov, A., Drewitt, J. W. E., Leydier, M., Thiaudière, D., Gruner, S., Brassamin, S., Zanghi, D., Cuello, G. J., Koza, M., Magazù, S., Greaves, G. N., and Price, D. L. (2011). Aerodynamic levitation and laser heating: applications at synchrotron and neutron sources. *Eur. Phys. J. Spec. Top.*, 196, 151–165.
- Hennet, L., Pozdnyakova, I., Bytchkov, A., Cristiglio, V., Palleau, P., Fischer, H. E., Cuello, G. J., Johnson, M., Melin, P., Zanghi, D., Brassamin, S., Brun, J.-F., Price, D. L., and Saboungi, M.-L. (2006). Levitation apparatus for neutron diffraction investigations on high temperature liquids. *Rev. Sci. Instrum.*, 77, article no. 053903.
- Hesse, K.-F. (1984). Refinement of the crystal structure of wollastonite-2M (parawollastonite). *Z. Für Krist.*, 168, 93–98.
- Howe, M. A., McGreevy, R. L., and Zetterström, P. (1996). CORRECT: a correction program for neutron diffraction data (NFL studsvik internal report).
- Jackson, W. E., Farges, F., Yeager, M., Mabrouk, P. A., Rossano, S., Waychunas, G. A., Solomon, E. I., and Brown, G. E. (2005). Multi-spectroscopic study of Fe(II) in silicate glasses: implications for the coordination environment of Fe(II) in silicate melts. *Geochim. Cosmochim. Acta*, 69, 4315–4332.
- Kalampounias, A. G., Nasikas, N. K., and Papatheodorou, G. N. (2009). Glass formation and structure in the $\text{MgSiO}_3\text{-Mg}_2\text{SiO}_4$ pseudobinary system: from degraded networks to ioniclike glasses. *J. Chem. Phys.*, 131, article no. 114513.
- Kohara, S., Akola, J., Morita, H., Suzuya, K., Weber, J. K. R., Wilding, M. C., and Benmore, C. J. (2011). Relationship between topological order and glass forming ability in densely packed enstatite and forsterite composition glasses. *Proc. Natl Acad. Sci. USA*, 108, 14780–14785.
- Kroeker, S. and Stebbins, J. F. (2000). Magnesium coordination environments in glasses and minerals: new insight from high-field magnesium-25 MAS NMR. *Am. Mineral.*, 85, 1459–1464.
- Labiche, J.-C., Mathon, O., Pascarelli, S., Newton, M. A., Ferre, G. G., Curfs, C., Vaughan, G., Homs, A., and Carreiras, D. F. (2007). The fast readout low noise camera as a versatile X-ray detector for time resolved dispersive extended X-ray absorption fine structure and diffraction studies of dynamic problems in materials science, chemistry, and catalysis. *Rev. Sci. Instrum.*, 78, article no. 091301.
- Le Losq, C. and Neuville, D. R. (2013). Effect of the Na/K mixing on the structure and the rheology of tectosilicate silica-rich melts. *Chem. Geol.*, 346, 57–71.
- Le Losq, C., Neuville, D. R., Chen, W., Florian, P., Massiot, D., Zhou, Z., and Greaves, G. N. (2017). Percolation channels: a universal idea to describe the atomic structure and dynamics of glasses and melts. *Sci. Rep.*, 7, article no. 16490.
- Majérus, O., Cormier, L., Calas, G., and Beuneu, B. (2004). A neutron diffraction study of temperature-induced structural changes in potassium disilicate glass and melt. *Chem. Geol.*, 213, 89–102.
- Matsubara, E., Kawazoe, T., Waseda, Y., Ashizuka, M., and Ishida, E. (1988). Oxygen coordination of magnesium and calcium in binary magnesia and calcia

- metaphosphate glasses. *J. Mater. Sci.*, 23, 547–550.
- Mysen, B. O. and Frantz, J. D. (1993). Structure and properties of alkali silicate melts at magmatic temperatures. *Eur. J. Mineral.*, 5, 393–408.
- Nasikas, N. K., Edwards, T. G., Sen, S., and Papatheodorou, G. N. (2012). Structural characteristics of novel Ca–Mg orthosilicate and suborthosilicate glasses: results from ^{29}Si and ^{17}O NMR spectroscopy. *J. Phys. Chem. B*, 116, 2696–2702.
- Neuville, D. R. and Richet, P. (1991). Viscosity and mixing in molten (Ca, Mg) pyroxenes and garnets. *Geochim. Cosmochim. Acta*, 55, 1011–1019.
- Nienhuis, E. T., Tuheen, M., Du, J., and McCloy, J. S. (2021). *In situ* pair distribution function analysis of crystallizing Fe-silicate melts. *J. Mater. Sci.*, 56, 5637–5657.
- Schneider, J., Mastelaro, V. R., Zanotto, E. D., Shakhmatkin, B. A., Vedishcheva, N. M., Wright, A. C., and Panepucci, H. (2003). Qn distribution in stoichiometric silicate glasses: thermodynamic calculations and ^{29}Si high resolution NMR measurements. *J. Non-Cryst. Solids*, 325, 164–178.
- Sen, S., Maekawa, H., and Papatheodorou, G. N. (2009). Short-range structure of invert glasses along the pseudo-binary join $\text{MgSiO}_3\text{--Mg}_2\text{SiO}_4$: results from ^{29}Si and ^{25}Mg MAS NMR spectroscopy. *J. Phys. Chem. B*, 113, 15243–15248.
- Shannon, R. D. (1976). Revised effective ionic radii and systematic studies of interatomic distance in halides and chalcogenides. *Acta Cryst.*, A32, 751–767.
- Shih, Y.-T., Sundararaman, S., Ispas, S., and Huang, L. (2021). New interaction potentials for alkaline earth silicate and borate glasses. *J. Non-Cryst. Solids*, 565, article no. 120853.
- Shimoda, K., Nemoto, T., and Saito, K. (2008). Local structure of magnesium in silicate glasses: a ^{25}Mg 3QMAS NMR study. *J. Phys. Chem. B*, 112, 6747–6752.
- Shimoda, K., Tobu, Y., Shimoikeda, Y., Nemoto, T., and Saito, K. (2007). Multiple Ca^{2+} environments in silicate glasses by high-resolution ^{43}Ca MQMAS NMR technique at high and ultra-high (21.8 T) magnetic fields. *J. Magn. Reson.*, 186, 156–159.
- Skinner, L. B., Benmore, C. J., Weber, J. K. R., Tumber, S., Lazareva, L., Neuefeind, J., Santodonato, L., Du, J., and Parise, J. B. (2012). Structure of molten CaSiO_3 : neutron diffraction isotope substitution with aerodynamic levitation and molecular dynamics study. *J. Phys. Chem. B*, 116, 13439–13447.
- Soper, A. K. (2005). Partial structure factors from disordered materials diffraction data: an approach using empirical potential structure refinement. *Phys. Rev. B*, 72, article no. 104204.
- Stebbins, J. F. (1995). Dynamics and structure of silicate and oxide melts: nuclear magnetic resonance studies. In Stebbins, J. F., McMillan, P. F., and Dingwell, D. B., editors, *Structure, Dynamics and Properties of Silicate Melts*. Mineralogical Society of America, Washington.
- Stebbins, J. F. (2008). Temperature effects on the network structure of oxide melts and their consequences for configurational heat capacity. *Chem. Geol.*, 256, 80–91.
- Taniguchi, T., Okuno, M., and Matsumoto, T. (1995). The structural studies of $\text{CaMgSi}_2\text{O}_6$, $\text{CaCoSi}_2\text{O}_6$ and $\text{CaNiSi}_2\text{O}_6$ glasses. *Mineral. J.*, 17, 231–244.
- Taniguchi, T., Okuno, M., and Matsumoto, T. (1997). X-ray diffraction and EXAFS studies of silicate glasses containing Mg, Ca and Ba atoms. *J. Non-Cryst. Solids*, 211, 56–63.
- Thompson, R. M. and Downs, R. T. (2003). Model pyroxenes I: ideal pyroxene topologies. *Am. Mineral.*, 88, 653–666.
- Thompson, R. M. and Downs, R. T. (2004). Model pyroxenes II: structural variation as a function of tetrahedral rotation. *Am. Mineral.*, 89, 614–628.
- Trojer, F. (1968). The crystal structure of parawollastonite. *Z. Für Krist.*, 127, 291–308.
- Waychunas, G. A., Brown, G. E., Ponader, C. W., and Jackson, W. E. (1988). Evidence from X-ray absorption for network-forming Fe^{2+} in molten alkali silicates. *Nature*, 332, 251–253.
- Weigel, C., Cormier, L., Calas, G., Galois, L., and Bowron, D. T. (2008). Intermediate-range order in the silicate network glasses $\text{NaFe}_x\text{Al}_{1-x}\text{Si}_2\text{O}_6$ ($x = 0, 0.5, 0.8, 1$): a neutron diffraction and empirical potential structure refinement modeling investigation. *Phys. Rev. B*, 78, article no. 064202.
- Wilding, M. C. and Benmore, C. J. (2006). Structure of glasses and melts. *Rev. Mineral. Geochem.*, 63, 275–311.
- Wilding, M. C., Benmore, C. J., Tangeman, J. A., and Sampath, S. (2004). Coordination changes in magnesium silicate glasses. *Eur. Lett.*, 67, 212–218.
- Wilding, M. C., Benmore, C. J., and Weber, J. K. R.

- (2008). *In situ* diffraction studies of magnesium silicate liquids. *J. Mater. Sci.*, 43, 4707–4713.
- Wilding, M. C., Benmore, C. J., and Weber, J. K. R. (2010). Changes in the local environment surrounding magnesium ions in fragile MgO–SiO₂ liquids. *Eur. Lett.*, 89, article no. 26005.
- Wright, A. C. (1993). The comparison of molecular dynamics simulations with diffraction experiments. *J. Non-Cryst. Solids*, 159, 264–268.
- Yin, C. D., Okuno, M., Morikawa, H., and Marumo, F. (1983). Structure analysis of MgSiO₃ glass. *J. Non-Cryst. Solids*, 55, 131–141.
- Zhang, P., Grandinetti, P. J., and Stebbins, J. F. (1997). Anionic species determination in CaSiO₃ glass using two-dimensional ²⁹Si NMR. *J. Phys Chem. B*, 101, 4004–4008.